Hole pocket–driven superconductivity and its universal features in the electron-doped cuprates

Li, Yangmu; Tabis, W.; Tang, Y.; Jaroszynski, J.; Barišić, Neven; Greven, M.

Source / Izvornik: **Science Advances, 2019, 5**

Journal article, Published version
Rad u časopisu, Objavljena verzija rada (izdavačev PDF)

https://doi.org/10.1126/sciadv.aap7349

Permanent link / Trajna poveznica: https://urn.nsk.hr/urn:nbn:hr:217:642919

CONDENSED MATTER PHYSICS

Hole pocket–driven superconductivity and its universal features in the electron-doped cuprates

Yangmu Li[1]*†, W. Tabis[1,2], Y. Tang[1], G. Yu[1], J. Jaroszynski[3], N. Barišić[1,4,5†], M. Greven[1†]

After three decades of intensive research attention, the emergence of superconductivity in cuprates remains an unsolved puzzle. One major challenge has been to arrive at a satisfactory understanding of the unusual metallic "normal state" from which the superconducting state emerges upon cooling. A second challenge has been to achieve a unified understanding of hole- and electron-doped compounds. Here, we report detailed magnetoresistance measurements for the archetypal electron-doped cuprate $Nd_{2-x}Ce_xCuO_{4+\delta}$ that, in combination with previous data, provide crucial links between the normal and superconducting states and between the electron- and hole-doped parts of the phase diagram. The characteristics of the normal state (magnetoresistance, quantum oscillations, and Hall coefficient) and those of the superconducting state (superfluid density and upper critical field) consistently indicate two-band (electron and hole) features and point to hole pocket–driven superconductivity in these nominally electron-doped materials. We show that the approximate Uemura scaling between the superconducting transition temperature and the superfluid density found for hole-doped cuprates also holds for the small hole component of the superfluid density in electron-doped cuprates.

INTRODUCTION

Superconductivity in the lamellar cuprates is achieved upon doping the quintessential CuO_2 sheets of parent spin-1/2 antiferromagnetic (AF) insulators such as La_2CuO_4 and Nd_2CuO_4 with either holes (*1*) or electrons (*2*). There has been a resurgence of interest in the electron-doped half of the phase diagram (*3*–*9*), where AF correlations are known to be more prominent (*10*–*12*). Hole carriers tend to occupy oxygen 2*p* orbitals, where they frustrate and quickly destroy long-range AF order, whereas electrons primarily enter copper 3*d* orbitals, where they gradually dilute the AF state (*10*). In a recent development, normal-state transport measurements revealed Fermi liquid (FL) properties in a wide temperature and doping range: (i) the sheet resistance follows an FL temperature-doping dependence in the pseudogap regime of the hole-doped cuprates (*13*, *14*) and in the AF phase of the electron-doped cuprates (*9*); (ii) the cotangent of the Hall angle is best understood in terms of a single FL scattering rate that is nearly independent of doping, compound, and charge-carrier type (*9*, *14*); (iii) the magnetoresistance (MR) obeys Kohler scaling in the pseudogap regime of the hole-doped materials, with an FL scattering rate (*15*); and (iv) the optical scattering rate exhibits temperature-frequency scaling expected for an FL system (*16*). These observations suggest that the transport properties of the cuprates may be understood by FL theory respecting the exact shape of the Fermi surface (FS).

Photoemission (*8*, *17*–*19*) and quantum oscillation (*6*, *7*, *20*) experiments performed on the electron-doped cuprates indicate several distinct FS topologies, as summarized for $Nd_{2-x}Ce_xCuO_{4+\delta}$ (NCCO) in Fig. 1: (1) at low doping, deep in the long-range–ordered AF (LR-AF) phase, only small electron pockets [around (π, 0) and equivalent] exist; (2) for bulk superconducting (SC) samples, at intermediate doping, both small electron and hole pockets [around (π/2, π/2) and equivalent] are observed. Although the AF correlations are short-ranged (*12*) and dynamic (*21*, *22*) in this part of the phase diagram, manifestations of the two-band FS are found in most physical properties. The states (1) and (2) appear to be separated by a "mixed-phase" region, where short-range static AF order and a depressed SC volume fraction are observed, likely as a result of an underlying first-order phase transition in the presence of structural inhomogeneity (e.g., the Nd/Ce substitutional inhomogeneity in the case of NCCO) observed by nuclear magnetic resonance and neutron scattering (*23*–*26*). Additional features of FS evolution were revealed for a number of electron-doped cuprates, such as NCCO and $Pr_{2-x}Ce_xCuO_{4+\delta}$ (PCCO) (*6*, *27*–*29*). For example, the Hall coefficient shows a sign change from negative to positive at intermediate doping (*6*, *30*), and the Seebeck coefficient has a positive contribution for SC samples (*29*). (3) Last, at high doping, a state with a large hole FS is expected (*17*, *31*), as indeed observed in recent photoemission work (*18*, *19*). The demarcations between these phases depend on the specific compound and choice of annealing conditions. For example, in $La_{2-x}Ce_xCuO_{4+\delta}$ (LCCO) films, the boundary between the AF and SC phases has been reported to be as low as x = 0.07, yet the nature of the phase transition appears to be the same as in NCCO and PCCO (*32*).

Shortly after the discovery of superconductivity in the electron-doped cuprates, Hirsch and Marsiglio proposed theoretically that hole carriers may be essential for superconductivity in these oxides (*33*). Dagan and Greene (*28*) subsequently studied the planar electrical resistivity (presumably dominated by electrons) and Hall angle (sensitive to both electrons and holes) for PCCO as a function of Ce concentration. They proposed hole superconductivity in the electron-doped cuprates based on the observation that, whereas the resistivity at temperatures much higher than the SC transition temperature T_c is insensitive to the emergence of superconductivity, the Hall angle can be used to identify the Ce concentration with the highest T_c. Yet no direct, quantitative connection was established among the appearance of hole carriers, the normal-state properties, and the SC-state characteristics.

Here, we combine new magnetotransport data for NCCO with published results to show that the normal-state properties and the

[1]School of Physics and Astronomy, University of Minnesota, Minneapolis, MN 55455, USA. [2]AGH University of Science and Technology, Faculty of Physics and Applied Computer Science, 30-059 Krakow, Poland. [3]National High Magnetic Field National Laboratory, Florida State University, 1800 E. Paul Dirac Drive, Tallahassee, FL 32310, USA. [4]Institute of Solid State Physics, TU Wien, 1040 Vienna, Austria. [5]Department of Physics, Faculty of Science, University of Zagreb, HR-10000 Zagreb, Croatia.
*Present address: Condensed Matter Physics and Materials Science Department, Brookhaven National Laboratory, Upton, NY 11973, USA.
†Corresponding author. Email: yangmuli@umn.edu (Y.L.); neven.barisic@tuwien.ac.at (N.B.); greven@umn.edu (M.G.)

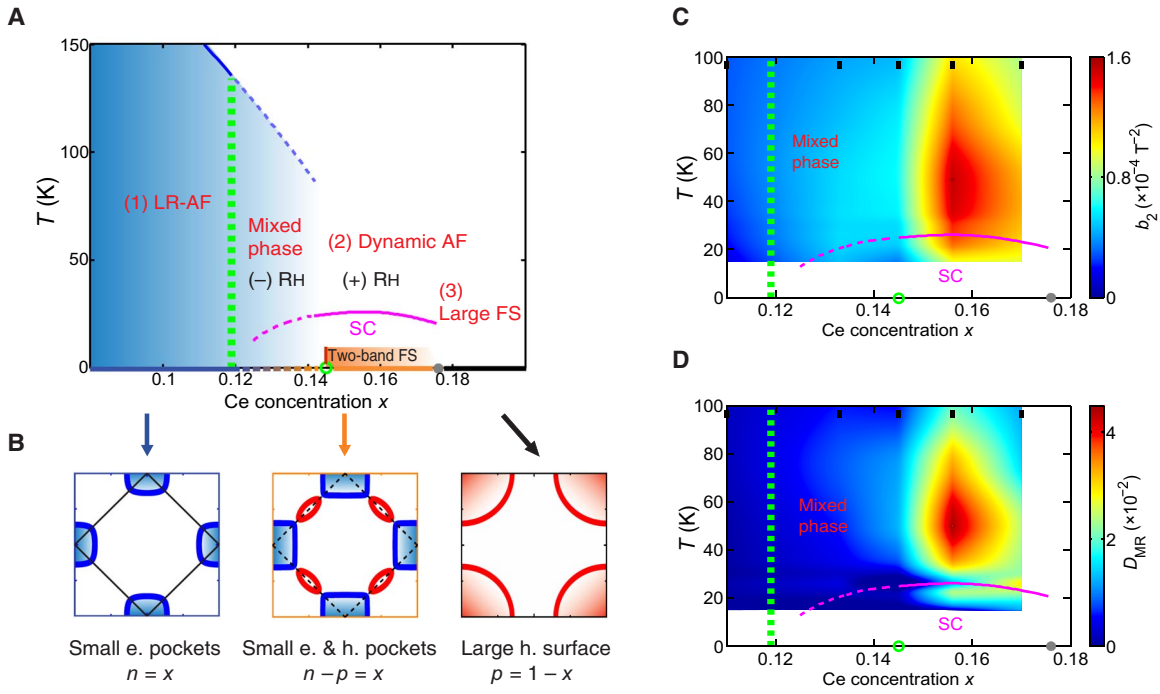

Fig. 1. Phase diagram and FS topologies. (**A**) Magnetic and electronic phase diagram for NCCO with standard reduction condition. The vertical green dashed line shows the boundary between the (1) LR-AF phase ($x < 0.12$) and the mixed-phase region with static short-range AF order and traces of superconductivity ($0.12 \leq x < 0.145$). The empty green circle signifies the Ce concentration at which (2) bulk superconductivity emerges and the magnetic response is purely dynamic ($0.145 \leq x < 0.175$) (*22*). A sign change in Hall coefficient is observed at $x = 0.145$ (*6*). The gray dot shows the estimated Ce concentration of the Lifshitz transition to a (3) state with a large hole FS ($x \geq 0.175$) (*6*, *17*, *18*, *20*, *31*). Solid and dashed lines on horizontal axis indicate distinct FS topologies described in (B). (**B**) FS topologies corresponding to the three doping ranges in (A). Solid ($x < 0.12$) and dashed ($0.145 \leq x < 0.175$) diagonal black lines indicate the LR-AF zone boundary and dynamic AF fluctuations, respectively. Blue and red curves indicate electron and hole FS, respectively. *n* and *p* are electron and hole carrier densities, respectively. Contour plot of (**C**) b_2 and (**D**) D_{MR}. A considerable increase in both b_2 and D_{MR} is observed above $x \approx 0.145$. Color scheme of the contour plots is chosen to emphasize these considerable increases. Black bars (top) indicate the Ce concentrations of the measured NCCO samples.

emergence of superconductivity are connected to the FS shape and to provide clear evidence for hole pocket–driven superconductivity in electron-doped cuprates. Our focus is on the states (1) and (2) and the intermediate mixed-phase region (Fig. 1). The MR magnitude [similar to the Hall angle in (*28*)] is a measure of the overall (hole and electron) FS curvature; it is small for a single, approximately circular FS, but substantial for a two-band (electron-hole) FS (see the Supplementary Materials). We observe a considerable increase in the MR magnitude at the Ce concentration where the small hole pockets and bulk superconductivity are first seen. The normal-state MR therefore reveals the underlying two-band FS topology and the emergent SC ground state. We then perform a quantitative analysis of the electron and hole contributions to the resistive upper critical field and the superfluid density of the bulk SC state. An important early discovery was that the hole-doped compounds below optimal doping exhibit approximately linear scaling between the superfluid density and T_c (*34*). After separating the two contributions to the superfluid density, we demonstrate that this approximately linear scaling extends to the hole superfluid density of electron-doped cuprates.

RESULTS

Representative transverse *ab*-plane MR data (current, *I*//*a*; magnetic field, *H*//*c*) are shown in Fig. 2. The longitudinal MR (*I*//*a* and *H*//*a*) is one order of magnitude smaller than the transverse MR (fig. S1) and thus not further considered here. The large difference in magnitude implies that the transverse *ab*-plane MR, discussed here in detail, is dominated by orbital contributions. We perform a quantitative analysis of the doping and temperature dependence of the MR using two distinct methods. The MR exhibits quadratic field dependence up to H_{dev} ~ 30 T and H_{dev} ~ 15 T for non-SC and SC samples, respectively. The exact field at which the MR deviates from quadratic field dependence depends on the temperature and doping level. We fit the data to $MR \equiv \Delta\rho/\rho(H=0) = b_2H^2$, where $\Delta\rho \equiv \rho(H) - \rho(H=0)$. $\rho(H=0)$ is the zero-field resistivity at $T > T_c$ and the extrapolated zero-field resistivity at $T \leq T_c$ ("method 1"). The coefficient b_2 is a measure of the MR magnitude. The deviation from quadratic field dependence at high fields ($H > H_{dev}$) is largest near optimal doping and indicative of a saturation effect due to the presence of small Fermi pockets. According to the classic theory of MR, deviation from quadratic field dependence appears when $\omega_c\tau$ becomes larger than unity (ω_c is the cyclotron frequency and τ is the relaxation time). The measured $H_{dev} \approx 30$ T for non-SC samples at low doping is consistent with the estimate $H_{dev} \approx 35 \pm 2.5$ T (at $T = 50$ K) based on the reported scattering rate (*9*) (see the Supplementary Materials). The observation of quantum oscillations requires $\omega_c\,\tau \gg 1$. At $H \approx 40$ T, quantum oscillations have only been observed in bulk SC samples ($H_{dev} \sim 15$ T) (*6*, *20*). We use the percentage difference, $D_{MR} \equiv (\rho_{H^2} - \Delta\rho)/\rho_{H^2}$, between the extrapolated quadratic behavior, $\rho_{H^2} = b_2H^2\rho(H=0)$, and the measured high-field MR, $\Delta\rho$, to characterize the magnitude of the deviation. Because

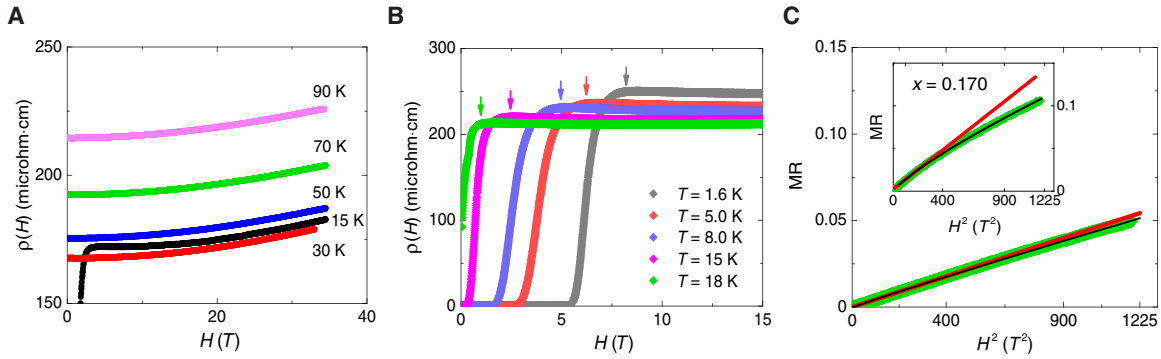

Fig. 2. Representative resistivity data. (**A**) Magnetic field dependence of the resistivity at a number of temperatures for NCCO with $x = 0.133$ and 0.170. For the $x = 0.133$ sample, a weak resistivity upturn in temperature can be seen below 30 K (*9*). (**B**) Resistivity data at $T < T_c$ for $x = 0.133$. The arrows indicate the field at which superconductivity is fully suppressed and the normal-state resistivity is recovered (resistive upper critical field). (**C**) MR (green) for $x = 0.133$ and 0.170 (inset) analyzed by two methods, as described in the main text (method 1: red lines; method 2: black lines).

the doping and temperature dependencies of D_{MR} are approximately independent of the field magnitude, we choose $H = 34.5$ T, the highest field used in our experiment, to calculate D_{MR}. An alternative approach ("method 2") is to fit the MR over the entire field range to a power-law behavior, $MR = b_n H^n$ (Fig. 2C). In this case, the coefficient b_n is a measure of MR magnitude, whereas $2 - n$ characterizes the magnitude of the deviation from the quadratic behavior. Both methods lead to the same conclusion that the normal-state MR and the SC emergence are related to the FS topology. We use method 1 in the main text and compare the two methods in the Supplementary Materials.

Contour plots of the coefficient b_2 and the high-field deviation D_{MR} are shown in Fig. 1 (C and D). Both quantities are nearly zero in the LR-AF phase ($x < 0.12$) and substantial for bulk SC materials ($0.145 \leq x < 0.175$), with a distinct increase at about $x = 0.145$. In the mixed-phase region ($0.12 \leq x < 0.145$), b_2 is nonzero and related to the SC volume fraction V_{SC} (estimated from magnetization measurements of polycrystalline samples obtained from the crystals used in MR measurements), as demonstrated in Fig. 3 (A and B). The contour plots of b_2 and D_{MR} can be directly compared to the evolution of FS topology (Fig. 1). Assuming a spatially uniform system, the doping dependence of b_2 can be calculated on the basis of the mean-field band structure and Boltzmann theory (see the Supplementary Materials). This calculation indicates that the hole pockets appear because of a decrease of the coherent AF backscattering amplitude with increasing doping [AF order gives rise to a gap at $(\pi/2, \pi/2)$]. Once the small hole pockets are present, a step-like increase is observed in b_2. The large values of b_2 and D_{MR} reflect a two-band FS in the normal state. In the archetypal cuprate NCCO, mesoscopic phase separation exists in the mixed-phase region, and the marked increase of V_{SC} near $x = 0.145$ tracks the doping dependence of b_2 (Fig. 3B). As seen from Fig. 3A, the normalized magnetic and SC volume fractions approximately add up to unity, which implies that the superconductivity in the mixed-phase region emerges from normal-state regions without static magnetic order.

The electronic ground state of the electron-doped cuprates depends not only on the Ce concentration but also on the postgrowth oxygen reduction conditions (*2*, *3*, *35*–*37*). In particular, superconductivity has not been observed in as-grown samples. The phase diagram in Fig. 1 pertains to NCCO subjected to standard oxygen reduction conditions (see Materials and Methods). Our measurements of NCCO with fixed Ce concentration ($x = 0.170$) show nearly zero MR (single-band FS) for an as-grown AF sample, and a large MR (two-band FS) for a reduced bulk SC sample (Fig. 3C). A previous study of the oxygen reduction effect on NCCO with $x = 0.15$ also found a strong correlation between the MR and the emergence of superconductivity (*30*). These observations suggest a robust connection between the two-band FS and bulk superconductivity, irrespective of the Ce content and oxygen reduction condition. Treating the doping level and reduction condition as implicit parameters (Fig. 3D) reveals a quantitative relation between the MR magnitude, normalized by the SC volume fraction, and T_c for a number of thin-film and bulk crystalline NCCO and PCCO samples.

The observation of a distinct signature of the two-band FS in the MR mandates that other properties should be analyzed accordingly. In particular, the upper critical field (H_{c2}) and the superfluid density (ρ_s), two characteristics of the SC ground state, may also exhibit two-band features (*38*, *39*). We estimate H_{c2} from our resistivity measurements upon fully suppressing superconductivity at low temperatures, with the magnetic field parallel to the crystalline *c* axis (Fig. 2B). As demonstrated in Fig. 4A, we observe a universal temperature dependence of the upper critical field for NCCO that is inconsistent with the behavior of a single-band Bardeen-Cooper-Schrieffer (BCS) superconductor. This universality implies that disorder effects (Nd/Ce and Cu/Ni substitution, differing oxygen reduction conditions) are not the main cause of the temperature dependence of H_{c2}. Instead, we find that the data are rather well described by a two-band FS model, analogous to MgB_2 and the iron-based superconductors (*40*, *41*). On the basis of measurements of the Nernst effect, it was argued that the resistive H_{c2} is lower than the "real" (Nernst) upper critical field (*42*). We show in the Supplementary Materials that H_{c2} estimated from the Nernst effect also cannot be described by a single-band BCS model, but that it can be consistently described by the two-band FS model.

Previous research on the electron-doped cuprates suggested that both electrons and holes contribute to the superfluid density $\rho_s \propto n/m^*$, where n is the normal-state carrier density and m^* is the effective mass (*39*). The electron-doped cuprates feature a nonmonotonic SC gap function with nodes at the hole pockets, but not at the electron pockets (*43*). The superfluid density for electrons therefore exhibits exponential temperature dependence $\rho_{s,e}(T) = \rho_{s,e}(0)(1 - e^{-\Delta/T+\Delta/T_e})$, where $\rho_{s,e}(0)$ and Δ are the zero-temperature electron superfluid density and the SC gap at electron pockets, respectively. For simplicity, the latter is assumed to be uniform, as it only changes moderately across electron pockets. T_e is the temperature at which $\rho_{s,e}$ becomes zero and does not necessarily equal T_c. Because of the existence of the gap node at the hole

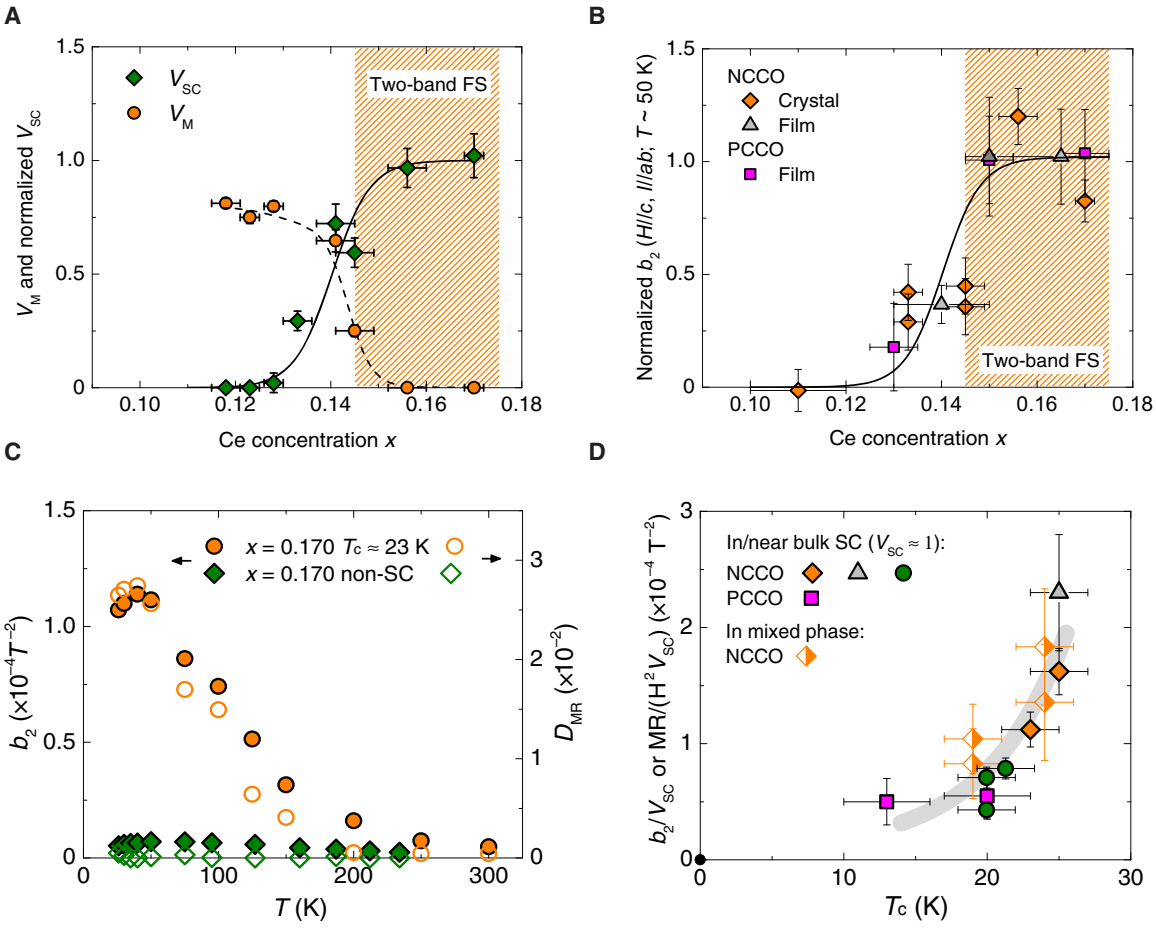

Fig. 3. Correlation between magnetoresistance and emergence of superconductivity. (**A**) SC and magnetic volume fractions as a function of Ce concentration. The former was obtained from magnetization data at 2 K, whereas the latter was obtained from μSR measurements at 40 K. As a result of doping the CuO_2 planes with electrons, the magnetic volume fraction has decreased to $V_M \approx 0.82$ at $x \approx 0.12$. Dashed and solid lines are guides to the eye. Shaded area indicates the doping range of the two-band FS. Data adopted from (*22*). (**B**) Normalized MR coefficient b_2 (b_2 normalized to 1 for samples with $x \approx 0.15$) as a function of Ce concentration. The symbol labels are the same as in (D). (**C**) Coefficients b_2 and D_{MR} for as-grown non-SC and reduced SC NCCO with $x = 0.170$. (**D**) MR normalized by SC volume fraction, shown as b_2/V_{SC} for samples measured in the present work and as $MR/(H^2V_{SC})$ for previous results. Orange diamonds: present work for NCCO; gray triangles (*51*) and green circles (*30*), NCCO films; purple squares, PCCO films (*27*). All the MR data in this figure were taken at $T \approx 50$ K. The full symbols indicate samples for which $V_{SC} \approx 1$ is estimated. The half symbols signify samples in the mixed phase. Error bars show estimated 1 SD.

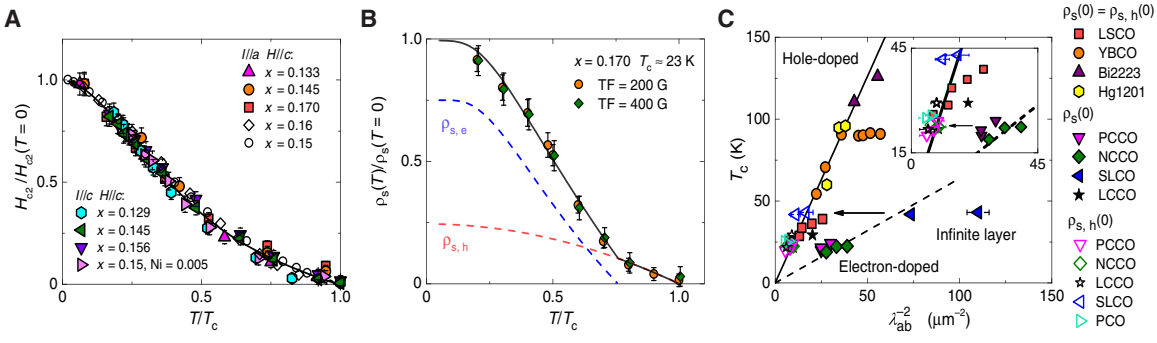

Fig. 4. Two-band upper critical field and superfluid density. (**A**) Universal temperature dependence of the resistive upper critical field for NCCO with *H//c*. The solid curve is a fit to the two-band model (see the Supplementary Materials). Published data taken from (*38*) ($x = 0.15$) and (*51*) ($x = 0.16$). (**B**) Temperature dependence of superfluid density extracted from transverse-field (TF) μSR measurements for a $x = 0.170$ sample (*22*). Fit of the two-band model, as described in the main text, is shown as a black solid line. Electron and hole contributions are plotted as blue and red dashed lines, respectively. (**C**) Universal scaling between $\rho_{s,h}(0)$ and T_c (black solid line). Black dashed line presents previous scaling (*34*) between $\rho_s(0)$ and T_c for the electron-doped cuprates. Both $\rho_{s,h}(0)$ and $\rho_s(0)$ are plotted as the inverse square of the penetration depth λ_{ab}. Data adopted from (*22*) (NCCO), (*44*) [PCCO, NCCO, and $Sr_{1-x}La_xCuO_2$ (SLCO)], (*48*) (SLCO), (*52*) [$La_{2-x}Sr_xCuO_4$ (LSCO), $YBa_2Cu_3O_y$ (YBCO), and $Bi_2Sr_2Ca_2Cu_3O_{10+\delta}$ (Bi2223)], (*53*) [$HgBa_2CuO_{4+\delta}$ (Hg1201)], and (*54*) (LCCO). The superfluid density of Ce-free $Pr_2CuO_{4\pm\delta}$ (PCO) samples subjected to special reduction conditions is estimated on the basis of measurements reported in (*14*). Note that the superfluid density of samples in the mixed phase can be somewhat smaller than the scaling result because of phase separation.

pockets, in the dirty limit, the superfluid density for holes exhibits a quadratic temperature dependence, $\rho_{s,h}(T) = \rho_{s,h}(0)(1 - T^2/T_h^2)$, where $\rho_{s,h}(0)$ is the zero-temperature hole superfluid density and T_h is the temperature at which the hole superfluid density vanishes. The total superfluid density, $\rho_s(T) = \rho_{s,e}(T) + \rho_{s,h}(T)$, was found to give a good description of previous data (*39*).

Representative superfluid density data, estimated from transverse-field muon spin rotation/relaxation measurements (μSR) for NCCO ($x = 0.17$), are shown in Fig. 4B. As in (*39*), we find that $\rho_s(T)$ can only be described by a quadratic temperature dependence near T_c and by a composite temperature dependence at low temperatures. From the fits, we obtain $\rho_{s,h}(0)/\rho_s(0) = 0.25 \pm 0.03$, and a more conservative estimate yields $\rho_{s,h}(0)/\rho_s(0) = 0.25 \pm 0.06$ (see Materials and Methods or the Supplementary Materials). This value is in reasonably good agreement with quantum oscillation measurements (for $x = 0.15$) that give normal-state electron and hole carrier densities of about 0.18 and 0.03, respectively (*20*). Upon considering the different effective masses of electrons and holes ($m^*_{hole} \approx 0.9m_e$, $m^*_{electron} \approx 2m_e$, where m_e is the electron free mass) (*9*, *14*, *20*), this implies that $\rho_{s,h}(0)/\rho_s(0) \approx 0.27$. Similarly, for PCCO, it was reported (*39*) that $\rho_{s,h}(0)/\rho_s(0) \approx 0.2$. Because data are only available for samples within a close doping range, and hence do not allow for a detailed study of the doping dependence of $\rho_{s,h}(0)/\rho_s(0)$, we assumed the same ratio for each compound (e.g., 0.27 for NCCO and 0.2 for PCCO). In early work, Uemura and colleagues observed a phenomenological universal linear scaling between $\rho_s(0)$ and T_c for underdoped holed-doped cuprates (*29*). An approximate linear scaling between these two observables was also found for the electron-doped cuprates (see Fig. 4C), but the distinct scaling ratios observed for hole- and electron-doped cuprates have remained unexplained (*44*). Upon separating electron and hole contributions, we show in Fig. 4C evidence for a universal scaling between $\rho_{s,h}(0)$ and T_c for both electron- and hole-doped cuprates.

DISCUSSION

The present MR data together with previous Hall-angle results (*28*) demonstrate that the emergence of superconductivity can be readily identified via normal-state charge transport measurements at temperatures much higher than T_c. This connection extends to other normal-state properties that are sensitive to the balance between hole and electron carrier density, e.g., Hall coefficient (*6*, *30*), Seebeck coefficient (*29*), optical conductivity (*31*), and quantum oscillations (*6*, *20*). The evolution of FS topology and the concomitant emergence of hole carriers, as captured by these normal-state charge transport measurements, are responsible for the appearance of a bulk SC phase. We note that connections between distinct electronic and structural characteristics and the emergence of superconductivity have already been reported in previous work (*23*–*26*). MR is a particularly sensitive probe of the emergence of superconductivity, as seen from our results for the mixed-phase region, in which transport properties are the result of a superposition of contributions from AF and SC (nonmagnetic) phases. In this region, we find that the MR of NCCO closely tracks the nonmagnetic volume fraction (comparable to V_{SC} at low temperature), whereas there has been no report of quantum oscillations, presumably because the typical nonmagnetic cluster size is smaller than the characteristic length scale (on the order of the cyclotron radius) associated with the quantum oscillations (*7*).

As shown in Fig. 4A, we observe a simple scaling of the reduced resistive upper critical field with T/T_c that is well described by a two-band (electron and hole) model. Given that the reduced resistive upper critical field for NCCO is largely independent of disorder type and amount, it is unlikely that the observed temperature dependence is dominated by disorder effects, but rather signifies a universal underlying characteristic of the doped CuO_2 planes of the electron-doped cuprates. Raman scattering experiments (*45*, *46*) also reveal that the coherent normal-state hole quasiparticles contribute to the superfluid density. Moreover, the superfluid response obtained from penetration depth measurements points to dual electron and hole contributions (*39*, *47*). Upon separating the electron and hole contributions to the superfluid density (Fig. 4B), we find that the data in Fig. 4C are consistent with a universal scaling between $\rho_{s,h}(0)$ and T_c for both electron- and hole-doped cuprates. This result points to a single underlying hole-related mechanism of superconductivity in the cuprates regardless of nominal carrier type. For the electron-doped cuprates, once a considerable portion of hole pairs have condensed into the SC state, electrons pairs begin to contribute as well (Fig. 4B).

The carrier density of the CuO_2 planes, and hence the FS of the electron-doped cuprates, can be modified by two methods: (i) chemical substitution (nominally tetravalent Ce for trivalent La, Nd, Pr, or Sm) and (ii) a postgrowth oxygen reduction process; both methods alter the disorder potential experienced by the CuO_2 planes (*2*, *3*, *8*, *35*–*37*). Our $x = 0.17$ NCCO MR data (Fig. 3C) along with the previous $x = 0.15$ NCCO result (*30*) show that a correlation between T_c and the normal-state MR exists in both cases. Recently, superconductivity was achieved in Ce-free thin-film samples via a special reduction procedure (*3*). Both the FS revealed by quantum oscillation measurements (the existence of small hole pockets) and the MR ($b_2 \sim 1.6 \times 10^{-4}$) for Ce-free thin-film samples of $Pr_2CuO_{4\pm\delta}$ are the same as for Ce-doped bulk SC samples subjected to standard oxygen reduction (*7*). These FS characteristics imply that these SC Ce-free thin-film samples are not undoped, but instead correspond to region (2) of the phase diagram (Fig. 1). Moreover, as shown in Fig. 4C, the estimated hole superfluid density obeys the universal scaling established here, indicative of the same SC ground state irrespective of reduction conditions.

The infinite-layer cuprates $Sr_{1-x}Ln_xCuO_2$ (Ln = La, Nd, Pr, and Sm) constitute a second family of electron-doped materials that differs structurally from the T′ family $Ln_{2-x}Ce_xCuO_4$ (Ln = La, Nd, Pr, Sm, Eu, and Gd). The exact symmetry of the SC wave function is under debate (see the Supplementary Materials), and the possible emergence of superconductivity from electron Fermi pockets was reported (*48*, *49*). In light of the fact that a hole contribution was deduced from the normal-state Hall constant of SC samples (*50*), we also considered the superfluid density of the infinite-layer cuprates. One way to understand the superfluid density of $Sr_{0.9}La_{0.1}CuO_2$ is to decompose it into *s*-wave and *d*-wave contributions (*48*). Assuming that the *s*-wave contribution is due to electrons and the *d*-wave contribution is due to holes, we show in Fig. 4C that the universal scaling seems to be obeyed as well.

MATERIALS AND METHODS

Sample preparation

The NCCO samples were synthesized using the traveling-solvent floating-zone technique in 4-atm Ar/O_2 and oriented by Laue diffraction within an angle of ±2°. Samples were reduced for 12 hours at 970°C in Ar flow and then treated for 20 hours at 500°C in oxygen flow. The onset SC transition temperature was determined from magnetization measurements using a Quantum Design Inc. Magnetic Property Measurement System and from resistivity measurements. The Ce concentration was

measured with inductively coupled plasma atomic emission spectroscopy and/or energy-dispersive x-ray spectroscopy. Approximately 1 mm of the surface of each crystal was removed to improve Ce homogeneity.

MR measurements and analysis

Single crystals of NCCO with $x = 0.110(10), 0.133(3), 0.145(4), 0.156(4)$, and 0.170(2) were measured using the four-contact method or in the Hall bar configuration. Measurements were performed with a Physical Property Measurement System (PPMS, up to 9 T; Quantum Design Inc.) at the University of Minnesota, and with a resistive magnet at the National High Magnetic Field Laboratory (dc field up to 34.5 T). The MR was determined in two principal geometries ($I//a$ and $H//a$; $I//a$ and $H//c$). For a few samples [$x = 0.133(3), 0.145(4), 0.156(4)$], the angular dependence was obtained. For simplicity, μ_0 and k_B are set to 1 throughout this work. For additional details, see the Supplementary Materials.

SUPPLEMENTARY MATERIALS

Supplementary material for this article is available at http://advances.sciencemag.org/cgi/content/full/5/2/eaap7349/DC1

Sample preparation

Table S1. NCCO sample information.

Supplementary Results and Discussion

Fig. S1. Longitudinal ($I//a$ and $H//a$) ab-plane MR.

Fig. S2. Comparison between two methods to analyze the MR.

Fig. S3. FS and calculation of the MR.

Fig. S4. Nernst upper critical field.

Fig. S5. Representative MR and H_{c2} data.

References (*55*–*60*)

REFERENCES AND NOTES

1. J. G. Bednorz, K. A. Müller, Possible high T_C superconductivity in the Ba-La-Cu-O system. *Z. Phys. B Condens. Matter* **64**, 189–193 (1986).
2. Y. Tokura, H. Takagi, S. Uchida, A superconducting copper oxide compound with electrons as the charge carriers. *Nature* **337**, 345–347 (1989).
3. Y. Krockenberger, H. Irie, O. Matsumoto, K. Yamagami, M. Mitsuhashi, A. Tsukada, M. Naito, H. Yamamoto, Emerging superconductivity hidden beneath charge-transfer insulators. *Sci. Rep.* **3**, 2235 (2013).
4. E. H. da Silva Neto, R. Comin, F. He, R. Sutarto, Y. Jiang, R. L. Greene, G. A. Sawatzky, A. Damascelli, Charge ordering in the electron-doped superconductor $Nd_{2-x}Ce_xCuO_4$. *Science* **347**, 282–285 (2015).
5. E. H. da Silva Neto, B. Yu, M. Minola, R. Sutarto, E. Schierle, F. Boschini, M. Zonno, M. Bluschke, J. Higgins, Y. Li, G. Yu, E. Weschke, F. He, M. Le Tacon, R. L. Greene, M. Greven, G. A. Sawatzky, B. Keimer, A. Damascelli, Doping-dependent charge order correlations in electron-doped cuprates. *Sci. Adv.* **2**, e1600782 (2016).
6. T. Helm, M. V. Kartsovnik, C. Proust, B. Vignolle, C. Putzke, E. Kampert, I. Sheikin, E.-S. Choi, J. S. Brooks, N. Bittner, W. Biberacher, A. Erb, J. Wosnitza, R. Gross, Correlation between Fermi surface transformations and superconductivity in the electron-doped high-T_c superconductor $Nd_{2-x}Ce_xCuO_4$. *Phys. Rev. B* **92**, 094501 (2015).
7. N. P. Breznay, R. D. McDonald, Y. Krockenberger, K. A. Modic, Z. Zhu, I. M. Hayes, N. L. Nair, T. Helm, H. Irie, H. Yamamoto, J. G. Analytis, Quantum oscillations suggest hidden quantum phase transition in the cuprate superconductor $Pr_2CuO_{4\pm\delta}$. arXiv:1510.04268 (2015).
8. M. Horio, T. Adachi, Y. Mori, A. Takahashi, T. Yoshida, H. Suzuki, L. C. C. Ambolode II, K. Okazaki, K. Ono, H. Kumigashira, H. Anzai, M. Arita, H. Namatame, M. Taniguchi, D. Ootsuki, K. Sawada, M. Takahashi, T. Mizokawa, Y. Koike, A. Fujimori, Suppression of the antiferromagnetic pseudogap in the electron-doped high-temperature superconductor by protect annealing. *Nat. Commun.* **7**, 10567 (2016).
9. Y. Li, W. Tabis, G. Yu, N. Barišić, M. Greven, Hidden Fermi-liquid charge transport in the antiferromagnetic phase of the electron-doped cuprates. *Phys. Rev. Lett.* **117**, 197001 (2016).
10. M. A. Kastner, R. J. Birgeneau, G. Shirane, Y. Endoh, Magnetic, transport, and optical properties of monolayer copper oxides. *Rev. Mod. Phys.* **70**, 897–928 (1998).
11. P. K. Mang, O. P. Vajk, A. Arvanitaki, J. W. Lynn, M. Greven, Spin correlations and magnetic order in nonsuperconducting $Nd_{2-x}Ce_xCuO_{4\pm\delta}$. *Phys. Rev. Lett.* **93**, 027002 (2004).
12. E. M. Motoyama, G. Yu, I. M. Vishik, O. P. Vajk, P. K. Mang, M. Greven, Spin correlations in the electron-doped high-transition-temperature superconductor $Nd_{2-x}Ce_xCuO_{4\pm\delta}$. *Nature* **445**, 186–189 (2007).
13. N. Barišić, M. K. Chan, Y. Li, G. Yu, X. Zhao, M. Dressel, A. Smontara, M. Greven, Universal sheet resistance and revised phase diagram of the cuprate high-temperature superconductors. *Proc. Natl. Acad. Sci. U.S.A.* **110**, 12235–12240 (2013).
14. N. Barišić, M. K. Chan, M. J. Veit, C. J. Dorow, Y. Ge, Y. Tang, W. Tabis, G. Yu, X. Zhao, M. Greven, Hidden Fermi-liquid behavior throughout the phase diagram of the cuprates. arXiv:1507.07885 (2015).
15. M. K. Chan, M. J. Veit, C. J. Dorow, Y. Ge, Y. Li, W. Tabis, Y. Tang, X. Zhao, N. Barišić, M. Greven, In-plane magnetoresistance obeys Kohler's rule in the pseudogap phase of cuprate superconductors. *Phys. Rev. Lett.* **113**, 177005 (2014).
16. S. I. Mirzaei, D. Stricker, J. N. Hancock, C. Berthod, A. Georges, E. van Heumen, M. K. Chan, X. Zhao, Y. Li, M. Greven, N. Barišić, D. van der Marel, Spectroscopic Evidence for a Fermi-liquid-like energy and temperature dependence of the relaxation rate in the pseudogap phase of the cuprates. *Proc. Natl. Acad. Sci. U.S.A.* **110**, 5774–5778 (2013).
17. N. P. Armitage, F. Ronning, D. H. Lu, C. Kim, A. Damascelli, K. M. Shen, D. L. Feng, H. Eisaki, Z.-X. Shen, P. K. Mang, N. Kaneko, M. Greven, Y. Onose, Y. Taguchi, Y. Tokura, Doping dependence of an n-type cuprate superconductor investigated by angle-resolved photoemission spectroscopy. *Phys. Rev. Lett.* **88**, 257001 (2002).
18. H. Matsui, T. Takahashi, T. Sato, K. Terashima, H. Ding, T. Uefuji, K. Yamada, Evolution of the pseudogap across the magnet-superconductor phase boundary of $Nd_{2-x}Ce_xCuO_4$. *Phys. Rev. B* **75**, 224514 (2007).
19. D. Song, G. Han, W. Kyung, J. Seo, S. Cho, B. S. Kim, M. Arita, K. Shimada, H. Namatame, M. Taniguchi, Y. Yoshida, H. Eisaki, S. R. Park, C. Kim, Electron number-based phase diagram of $Pr_{1-x}LaCe_xCuO_{4-\delta}$ and possible absence of disparity between electron- and hole-doped cuprate phase diagrams. *Phys. Rev. Lett.* **118**, 137001 (2017).
20. M. V. Kartsovnik, T. Helm, C. Putzke, F. Wolff-Fabris, I. Sheikin, S. Lepault, C. Proust, D. Vignolles, N. Bittner, W. Biberacher, Fermi surface of the electron-doped cuprate superconductor $Nd_{2-x}Ce_xCuO_4$ probed by high-field magnetotransport. *New J. Phys.* **13**, 015001 (2011).
21. G. M. Luke, L. P. Le, B. J. Sternlieb, Y. J. Uemura, J. H. Brewer, R. Kadono, R. F. Kiefl, S. R. Kreitzman, T. M. Riseman, C. E. Stronach, M. R. Davis, S. Uchida, H. Takagi, Y. Tokura, Y. Hidaka, T. Murakami, J. Gopalakrishnan, A. W. Sleight, M. A. Subramanian, E. A. Early, J. T. Markert, M. B. Maple, C. L. Seaman, Magnetic order and electronic phase diagrams of electron-doped copper oxide materials. *Phys. Rev. B* **42**, 7981–7988 (1990).
22. Y. Li, "Neutron scattering, muon spin rotation/relaxation, and charge transport study of the electron-doped cuprate superconductors," thesis, University of Minnesota (2017).
23. M. Abe, K. Kumagai, S. Awaji, T. Fujita, Cu-NMR studies of $Nd_{2-x}Ce_xCuO_{4-y}$. *Physica C Supercond.* **160**, 8–16 (1989).
24. W. Henggeler, G. Cuntze, J. Mesot, M. Klauda, G. Saemann-Ischenko, A. Furrer, Neutron spectroscopic evidence for cluster formation and percolative superconductivity in $Pr_{2-x}Ce_xCuO_{4-\delta}$ ($0 \le x \le 0.2$). *Europhys. Lett.* **29**, 233–238 (1995).
25. S. J. L. Billinge, T. Egami, Short-range atomic structure of $Nd_{2-x}Ce_xCuO_{4-y}$ determined by real-space refinement of neutron-powder-diffraction data. *Phys. Rev. B* **47**, 14386–14406 (1993).
26. P. Lightfoot, D. R. Richards, B. Dabrowski, D. G. Hinks, S. Pei, D. T. Marx, A. W. Mitchell, Y. Zhang, J. D. Jorgensen, Phase separation in $Nd_{2-x}Ce_xCuO_4$. *Physica C Supercond.* **168**, 627–636 (1990).
27. P. Li, F. F. Balakirev, R. L. Greene, High-Field Hall Resistivity and Magnetoresistance of Electron-Doped $Pr_{2-x}Ce_xCuO_{4-\delta}$. *Phys. Rev. Lett.* **99**, 047003 (2007).
28. Y. Dagan, R. L. Greene, Hole superconductivity in the electron-doped superconductor $Pr_{2-x}Ce_xCuO_4$. *Phys. Rev. B* **76**, 024506 (2007).
29. X.-Q. Xu, S. J. Hagen, W. Jiang, J. L. Peng, Z. Y. Li, R. L. Greene, Thermoelectric power of $Nd_{2-x}Ce_xCuO_4$ crystals. *Phys. Rev. B* **45**, 7356–7359 (1992).
30. J. Wu, S. N. Mao, X. X. Xi, X. Jiang, J. L. Peng, T. Venkatesan, C. J. Lobb, R. L. Greene, Anomalous transport properties in superconducting $Nd_{1.85}Ce_{0.15}CuO_{4\pm\delta}$. *Phys. Rev. Lett.* **73**, 1291–1294 (1994).
31. Y. Onose, Y. Taguchi, K. Ishizaka, Y. Tokura, Doping dependence of pseudogap and related charge dynamics in $Nd_{2-x}Ce_xCuO_4$. *Phys. Rev. Lett.* **87**, 217001 (2001).
32. H. Saadaoui, Z. Salman, H. Luetkens, T. Prokscha, A. Suter, W. A. MacFarlane, Y. Jiang, K. Jin, R. L. Greene, E. Morenzoni, R. F. Kiefl, The phase diagram of electron-doped $La_{2-x}Ce_xCuO_{4-\delta}$. *Nat. Commun.* **6**, 6041 (2015).
33. J. E. Hirsch, F. Marsiglio, Hole superconductivity: Review and some new results. *Physica C* **162–164**, 591–598 (1989).
34. Y. J. Uemura, G. M. Luke, B. J. Sternlieb, J. H. Brewer, J. F. Carolan, W. N. Hardy, R. Kadono, J. R. Kempton, R. F. Kiefl, S. R. Kreitzman, P. Mulhern, T. M. Riseman, D. L. I. Williams, B. X. Yang, S. Uchida, H. Takagi, J. Gopalakrishnan, A. W. Sleight, M. A. Subramanian, C. L. Chien, M. Z. Cieplak, G. Xiao, V. Y. Lee, B. W. Statt, C. E. Stronach, W. J. Kossler, X. H. Yu, Universal correlations between T_c and $\frac{n_s}{m^*}$ (carrier density over effective mass) in high-T_c cuprate superconductors. *Phys. Rev. Lett.* **62**, 2317–2320 (1989).

35. P. K. Mang, S. Larochelle, A. Mehta, O. P. Vajk, A. S. Erickson, L. Lu, W. J. L. Buyers, A. F. Marshall, K. Prokes, M. Greven, Phase decomposition and chemical inhomogeneity in $Nd_{2-x}Ce_xCuO_{4+\delta}$. *Phys. Rev. B* **70**, 094507 (2004).
36. H. J. Kang, P. Dai, B. J. Campbell, P. J. Chupas, S. Rosenkranz, P. L. Lee, Q. Huang, S. Li, S. Komiya, Y. Ando, Microscopic annealing process and its impact on superconductivity in T′-structure electron-doped copper oxides. *Nat. Mat.* **6**, 224 (2007).
37. J. S. Higgins, Y. Dagan, M. C. Barr, B. D. Weaver, R. L. Greene, Role of oxygen in the electron-doped superconducting cuprates. *Phys. Rev. B* **73**, 104510 (2006).
38. T. B. Charikova, N. G. Shelushinina, G. I. Harus, D. S. Petukhov, V. N. Neverov, A. A. Ivanov, Upper critical field in electron-doped cuprate superconductor $Nd_{2-x}Ce_xCuO_{4+\delta}$: Two-gap model. *Physica C* **488**, 25–29 (2013).
39. H. G. Luo, T. Xiang, Superfluid response in electron-doped cuprate superconductors. *Phys. Rev. Lett.* **94**, 027001 (2005).
40. A. Gurevich, Enhancement of the upper critical field by nonmagnetic impurities in dirty two-gap superconductors. *Phys. Rev. B* **67**, 184515 (2003).
41. F. Hunte, J. Jaroszynski, A. Gurevich, D. C. Larbalestier, R. Jin, A. S. Sefat, M. A. McGuire, B. C. Sales, D. K. Christen, D. Mandrus, Two-band superconductivity in $LaFeAsO_{0.89}F_{0.11}$ at very high magnetic fields. *Nature* **453**, 903–905 (2008).
42. Y. Wang, S. Ono, Y. Onose, G. Gu, Y. Ando, Y. Tokura, S. Uchida, N. P. Ong, Dependence of upper critical field and pairing strength on doping in cuprates. *Science* **299**, 86–89 (2003).
43. G. Blumberg, A. Koitzsch, A. Gozar, B. S. Dennis, C. A. Kendziora, P. Fournier, R. L. Greene, Nonmonotonic $d_{x^2-y^2}$ superconducting order parameter in $Nd_{2-x}Ce_xCuO_4$. *Phys. Rev. Lett.* **88**, 107002 (2002).
44. H. Luetkens, H.-H. Klauss, R. Khasanov, A. Amato, R. Klingeler, I. Hellmann, N. Leps, A. Kondrat, C. Hess, A. Köhler, G. Behr, J. Werner, B. Büchner, Field and temperature dependence of the superfluid density in $LaFeAsO_{1-x}F_x$ superconductors: A muon spin relaxation study. *Phys. Rev. Lett.* **101**, 097009 (2008).
45. M. M. Qazilbash, A. Koitzsch, B. S. Dennis, A. Gozar, H. Balci, C. A. Kendziora, R. L. Greene, G. Blumberg, Evolution of superconductivity in electron-doped cuprates: Magneto-Raman spectroscopy. *Phys. Rev. B* **72**, 214510 (2005).
46. C. S. Liu, H. G. Luo, W. C. Wu, T. Xiang, Two-band model of Raman scattering on electron-doped high-T_c superconductors. *Phys. Rev. B* **73**, 174517 (2006).
47. T. Das, R. S. Markiewicz, A. Bansil, Nodeless *d*-wave superconducting pairing due to residual antiferromagnetism in underdoped $Pr_{2-x}Ce_xCuO_{4-\delta}$. *Phys. Rev. Lett.* **98**, 197004 (2007).
48. R. Khasanov, A. Shengelaya, A. Maisuradze, D. Di Castro, I. M. Savić, S. Weyeneth, M. S. Park, D. J. Jang, S.-I. Lee, H. Keller, Nodeless superconductivity in the infinite-layer electron-doped cuprate superconductor $Sr_{0.9}La_{0.1}CuO_2$. *Phys. Rev. B* **77**, 184512 (2008).
49. J. W. Harter, L. Maritato, D. E. Shai, E. J. Monkman, Y. Nie, D. G. Schlom, K. M. Shen, Nodeless superconducting phase arising from a strong (π, π) antiferromagnetic phase in the infinite-layer electron-doped $Sr_{1-x}La_xCuO_2$ Compound. *Phys. Rev. Lett.* **109**, 267001 (2012).
50. L. Fruchter, F. Bouquet, Z. Z. Li, Electric-field effect on electron-doped infinite-layer $Sr_{0.88}La_{0.12}CuO_{2+x}$ thin films. *Phys. Rev. B* **84**, 092502 (2011).
51. F. Gollnik, M. Naito, Doping dependence of normal- and superconducting-state transport properties of $Nd_{2-x}Ce_xCuO_{4\pm y}$ thin films. *Phys. Rev. B* **58**, 11734 (1998).
52. Y. J. Uemura, L. P. Le, G. M. Luke, B. J. Sternlieb, W. D. Wu, J. H. Brewer, T. M. Riseman, C. L. Seaman, M. B. Maple, M. Ishikawa, D. G. Hinks, J. D. Jorgensen, G. Saito, H. Yamochi, Basic similarities among cuprate, bismuthate, organic, Chevrel-phase, and heavy-fermion superconductors shown by penetration-depth measurements. *Phys. Rev. Lett.* **66**, 2665–2668 (1991).
53. C. Panagopoulos, T. Xiang, W. Anakool, J. R. Cooper, Y. S. Wang, C. W. Chu, Superfluid response in monolayer high-T_c cuprates. *Phys. Rev. B* **67**, 220502(R) (2003).
54. J. A. Skinta, M.-S. Kim, T. R. Lemberger, T. Greibe, M. Naito, Evidence for a transition in the pairing symmetry of the electron-doped cuprates $La_{2-x}Ce_xCuO_{4-y}$ and $Pr_{2-x}Ce_xCuO_{4-y}$. *Phys. Rev. Lett.* **88**, 207005 (2002).
55. J. Lin, A. J. Millis, Theory of low-temperature Hall effect in electron-doped cuprates. *Phys. Rev. B* **72**, 214506 (2005).
56. O. K. Anderson, A. I. Liechtenstein, O. Jepsen, F. Paulsen, LDA energy bands, low-energy hamiltonians, *t′*,*t* ″, $t_\perp$ (k), and $J_\perp$. *J. Phys. Chem. Solids* **56**, 1573–1591 (1995).
57. F. J. Blatt, *Physics of Electronic Conduction in Solids* (McGraw-Hill, 1968).
58. J. G. Storey, Hall effect and Fermi surface reconstruction via electron pockets in the high-T_c cuprates. *Europhys. Lett.* **113**, 27003 (2016).
59. M. Lambacher, "Crystal growth and normal state transport of electron-dopedhigh-temperature superconductors," thesis, Technische Universität München (2008).
60. F. F. Tafti, F. Laliberté, M. Dion, J. Gaudet, P. Fournier, L. Taillefer, Nernst effect in the electron-doped cuprate superconductor $Pr_{2-x}Ce_xCuO_4$: Superconducting fluctuations, upper critical field H_{c2}, and the origin of the T_c dome. *Phys. Rev. B* **90**, 024519 (2014).

Acknowledgments: We thank E. M. Motoyama for the growth of some of the NCCO samples, I. M. Vishik for the growth of the Ni-doped NCCO sample, T. Peterson for assistance with the operation of the Quantum Design Inc. PPMS system, and J. Cai for help with the MR calculations. We gratefully acknowledge helpful discussions with A. V. Chubukov, R. L. Greene, J. Kang, E. H. da Silva Neto, I. M Vishik, and X. Wang. **Funding:** This work was supported partially by the National Science Foundation (NSF) through the University of Minnesota MRSEC under grant no. DMR-1420013 and by NSF grant no. 1006617. The work at the TU Wien was supported by FWF project no. P27980-N36 and the European Research Council (ERC consolidator grant no. 725521). A portion of this work was performed at the National High Magnetic Field Laboratory, which is supported by NSF cooperative agreement no. DMR-1157490 and the State of Florida. **Author contributions:** Y.L., N.B., and M.G. conceived the research. Y.L., W.T., and G.Y. prepared the samples for transport measurements. Y.L., N.B., W.T., Y.T., and J.J. carried out the measurements at the NMHFL. Y.L. and W.T. carried out in-house magnetoresistance measurements. Y.L. performed data analysis and calculations guided by N.B. and M.G. Y.L., N.B., and M.G. wrote the manuscript with input from all authors. **Competing interests:** The authors declare that they have no competing interests. **Data and materials availability:** All data needed to evaluate the conclusions in the paper are present in the paper and/or the Supplementary Materials. Additional data related to this paper may be requested from the authors.

Submitted 22 August 2017
Accepted 2 October 2018
Published 1 February 2019
10.1126/sciadv.aap7349

Citation: Y. Li, W. Tabis, Y. Tang, G. Yu, J. Jaroszynski, N. Barišić, M. Greven, Hole pocket–driven superconductivity and its universal features in the electron-doped cuprates. *Sci. Adv.* **5**, eaap7349 (2019).

Hole pocket–driven superconductivity and its universal features in the electron-doped cuprates

Yangmu Li, W. Tabis, Y. Tang, G. Yu, J. Jaroszynski, N. Barisic and M. Greven

Sci Adv **5** (2), eaap7349.
DOI: 10.1126/sciadv.aap7349